Spatial variations of effective elastic thickness of the lithosphere in Central America and surrounding regions

Alberto Jiménez-Díaz , Javier Ruiz , Marta Pérez-Gussinyé , Jon F. Kirby , José A. Álvarez-Gómez , Rosa Tejero , Ramón Capote

Keywords:
effective elastic thickness
spectral methods
lithosphere structure
Central America
Caribbean plate

ABSTRACT

As a proxy for long-term lithospheric strength, the effective elastic thickness (T_e) can be used to understand the relationship between lithospheric rheology and geodynamic evolution of complex tectonic settings. Here we present, for the first time, high-resolution maps of spatial variations of T_e in Central America and surrounding regions from the analysis of the coherence between topography and Bouguer gravity anomaly using multitaper and wavelet methods. Regardless of the technical differences between the two methods, there is a good overall agreement in the spatial variations of T_e recovered from both methods. Although absolute T_e values can vary in both maps, the qualitative T_e structure and location of the main T_e gradients are very similar. The pattern of the T_e variations in Central America and surrounding regions agrees well with the tectonic provinces in the region, and it is closely related to major tectonic boundaries, where the Middle American and Lesser Antilles subduction zones are characterized by a band of high T_e on the downgoing slab seaward of the trenches. These high T_e values are related to internal loads (and in the case of the southernmost tip of the Lesser Antilles subduction zone also associated with a large amount of sediments) and should be interpreted with caution. Finally, there is a relatively good correlation, despite some uncertainties, between surface heat flow and our T_e results for the study area. These results suggest that although this area is geologically complex, the thermal state of the lithosphere has profound influence on its strength, such that T_e is strongly governed by thermal structure.

1. Introduction

The knowledge of lateral variations in lithosphere strength can aid in understanding how surface deformation relates to deep Earth processes. As a proxy for long-term lithospheric strength, the effective elastic thickness of the lithosphere (T_e) corresponds to the thickness of an idealized elastic plate bending under the same applied loads (Watts, 2001), and is related to the integrated mechanical strength of the lithosphere (Burov and Diament, 1995). The knowledge of T_e in different places provides a measurement of the spatial variation of the lithospheric strength, which is strongly controlled by local and regional conditions. Although T_e does not represent an actual depth to the base of the mechanical lithosphere, its spatial variations reflect relative lateral variations in lithospheric mechanical thickness (see McNutt, 1984). Thus it can be used to understand the relationship between lithospheric rheology and geodynamic evolution of complex tectonic settings.

T_e primarily depends on the thickness and structure of the crust, the composition of the crust and the lithospheric mantle, the degree of their coupling, the thermal state of the lithosphere, the state of stress, plate curvature, and the presence of melts, fluids and faults (e.g., Lowry and Smith, 1995; Burov and Diament, 1995; Lowry et al., 2000; Watts, 2001; Artemieva, 2011). The oceanic lithosphere generally behaves like a single mechanical layer due to the thin crust, which is usually coupled to the lithospheric mantle, and T_e is to first order controlled by the thermal age of the lithosphere at the time of loading (Watts, 2001; Kalnins and Watts, 2009). By contrast, the thermal state and rheological behavior of the lithosphere in continental areas are largely a consequence of local conditions (e.g., Ranalli, 1997; Afonso and Ranalli, 2004; Bürgmann and Dresen, 2008; Hasterok and Chapman, 2011; Mareschal and Jaupart, 2013), such that there is a complex relationship between T_e and its controlling parameters (Watts and Burov, 2003; Burov and Watts, 2006; Burov, 2011).

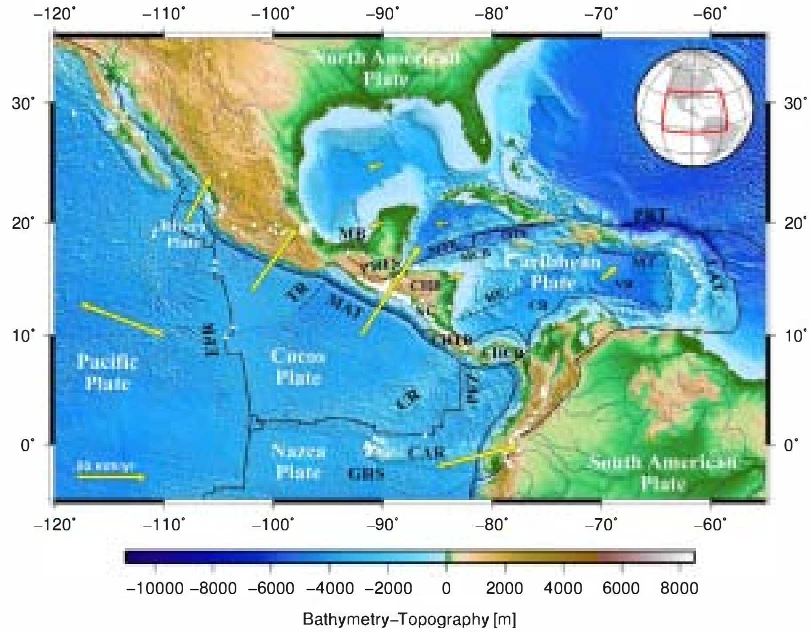

Fig. 1. Geotectonic setting of Central America and surrounding regions. Shaded relief image of bathymetry and topography is from ETOPO1 digital data (Amante and Eakins, 2009), and boundaries of lithospheric plates are based on the PB2002 model (Bird, 2003). Yellow arrows denote vectors of the plate motion from the MORVEL model (DeMets et al., 2010) with respect to the NNR reference frame as calculated at the given position with the Plate Motion Calculator (http://www.unavco.org/community_science/science-support/crustal_motion/dxdt/model.html). Triangles show the position of Holocene volcanoes (Siebert and Simkin, 2002). Abbreviations: CAR, Carnegie Ridge; CB, Colombian Basin; CHB, Chortis Block; CHCB, Chocó Block; CHTB, Choretega Block; CR, Cocos Ridge; EPR, East Pacific Rise; GHS, Galápagos Hotspot; HE, Hess Escarpment; LAT, Lesser Antilles Trench; MAT, Middle America Trench; MB, Maya Block; MCR, Mid-Cayman Rise; MT, Muertos Trough; ND, Nicaraguan Depression; OTF, Oriente Transform Fault; PFZ, Panamá Fracture Zone; PMFS, Polochic–Motagua Fault System; PRT, Puerto Rico Trench; SITF, Swan Island Transform Fault; TR, Tehuantepec Ridge; VB, Venezuelan Basin. (For interpretation of the references to color in this figure legend, the reader is referred to the web version of this article.)

In this study we present, for the first time, high-resolution maps of spatial variations of T_e in Central America and surrounding regions from the analysis of the Bouguer coherence using both multitaper and wavelet methods. The Central America–Caribbean region is characterized by the interaction of six lithospheric plates (Fig. 1). The Caribbean plate moves eastward relative to its two neighboring plates, North and South America plates (DeMets et al., 2010), and its perimeter is characterized by a high variability and complexity of geodynamic and tectonic processes (e.g., Sykes et al., 1982; Ross and Scotese, 1988). Therefore, this area represents a good natural laboratory to study the spatial variations of T_e, test the response of spectral methods to different factors and geodynamic conditions, and examine relationships between surface deformation, lithospheric structure and mantle dynamics.

In the following sections we first introduce the methodology and data employed for estimating T_e. We then present our results and compare them to previous estimates of T_e in the study area. Finally, we examine the relationships between T_e with other proxies for lithospheric and sub-lithospheric structure to improve our knowledge of the long-term rheology and mechanical behavior of the lithosphere in the study area. We also discuss how the lithospheric structure derived from our T_e analysis relates to surface deformation.

2. T_e estimation by spectral methods

To estimate the effective elastic thickness we calculate the coherence function relating the topography and Bouguer anomaly, commonly known as Bouguer coherence, using multitaper and wavelet methods. This function gives information on the wavelength band over which topography and Bouguer anomaly are correlated. In the coherence deconvolution method of Forsyth (1985), T_e is estimated by comparing the observed coherence curve with coherence functions predicted for a range of T_e values. For each given T_e, we calculate via deconvolution the initial surface and subsurface loads and compensating deflections that generate a predicted topography and gravity that best fit the observed topography and gravity anomaly, and a predicted coherence that best fits the observed coherence (Forsyth, 1985). The T_e value that minimizes the differences between the predicted and observed quantities is the optimal one for the analyzed area. The Bouguer coherence generally tends to zero at short wavelengths, where the topography is not compensated and loads are supported predominantly by the elastic strength of the lithosphere (Forsyth, 1985). At long wavelengths, the response to loading approaches the Airy limit and the coherence tends to one. The wavelengths at which the coherence rapidly increases from 0 to 1 depend on the effective elastic thickness of the lithosphere, such that when the lithosphere is weak and T_e is small, local compensation for loading occurs at relatively shorter wavelengths and vice versa.

In this section we describe briefly the methodology and data employed to estimate T_e. For an extensive description of the methods, choice of parameters and biases in T_e estimation, see Supplementary Material associated with the online version of this article.

2.1. Multitaper method

To recover spatial variations in T_e we divide the analysis area into overlapping windows, such that in each window the coherence is calculated and inverted assuming a spatially constant T_e, moving the centre of each window 50 km for each new estimate. Calculation of the observed and predicted coherence involves transformation into the Fourier domain of the topography and Bouguer gravity anomaly to estimate their auto- and cross-power spectra. Because both data sets are non-periodic and finite, the Fourier transformation presents problems of frequency leakage (Thomson, 1982; Simons et al., 2000), resulting in estimated spectra that differ from the true spectra. To reduce leakage, the data are first multiplied by a set of orthogonal tapers in the space domain, the Fourier transform of the data-taper product taken for each taper, and the power spectrum determined at each taper. The final estimate of the signal's true power spectrum is then the weighted average of the individual power spectra over all tapers. However, the choice of taper influences the resulting power spectra and hence the coherence function (Pérez-Gussinyé et al. 2007, 2008). The set of orthogonal tapers is defined by the bandwidth product NW that controls the wavelength resolution and spectral leakage (where N is the number of samples within the data window and W is the half bandwidth of the central lobe of the power spectral density of the first-order taper) and by the number of tapers K that governs the estimation variance (see Simons et al., 2000). The choice of bandwidth parameter NW in the multitaper technique is important. As the bandwidth increases, the resolution (i.e. the minimum separation in wave number between approximately uncorrelated spectral estimates) decreases (Walden et al., 1995). For a given bandwidth, W, there are up to $K = 2NW - 1$ tapers with good leakage properties (Percival and Walden, 1993). The variance of the spectral estimates decreases with the number of tapers as $1/K$, so the bandwidth and resolution are chosen depending on the individual function under analysis (Percival and Walden, 1993). In this study we apply the multitaper method using $NW = 3$ and $K = 3$, which are also used in several recent studies for T_e estimation (see e.g. Daly et al., 2004; Audet et al., 2007; Pérez-Gussinyé et al., 2009a; Kirby and Swain, 2011).

The effect of calculating T_e within a finite-size window is to limit the maximum wavelength of the gravity and topography that can be recovered. The choice of window size is critical in the multitaper estimation of T_e because it compromises the trade-off between resolution and variance of the estimates (Pérez-Gussinyé et al., 2004; Audet et al., 2007), such that large windows are better able to retrieve high T_e but degrade the spatial resolution and potentially merge tectonic provinces, while small windows provide high spatial resolution and analyze perhaps just one province but cannot resolve long flexural wavelengths. As the resulting T_e estimate depends on window size, we use three different window sizes (400×400 km, 600×600 km and 800×800 km, respectively) to obtain high spatial resolution and at the same time recover potentially high T_e. Finally, the T_e results estimated from three different window sizes are merged to obtain the final T_e map. This is done by calculating a weighted average of the T_e estimated from each of the three windows following the approach of Pérez-Gussinyé et al. (2009b). This approach combines the information content regarding abrupt T_e gradients recovered by small windows and the more reliable information on high T_e recovered by the larger windows.

2.2. Wavelet method

The wavelet method convolves a range of scaled wavelets with the whole data set to map and invert the coherence at each grid point, and achieves good wavenumber resolution over long length scales and good spatial resolution over short length scales. Here we employ a Morlet wavelet of high spatial resolution in the fan wavelet transform (Kirby and Swain, 2011). The value of the central wavenumber of the Morlet wavelet, denoted by $|\mathbf{k}_0|$, governs the resolution of the wavelet in the space and wavenumber domains. Larger values of $|\mathbf{k}_0|$ give better wavenumber resolution but poorer spatial resolution, and vice versa for smaller values (Addison, 2002). The choice of the value of $|\mathbf{k}_0|$, described in Kirby and Swain (2011), is governed by the amplitude of the first sidelobes of the simple wavelet. If this amplitude is a fraction $1/p$ ($p > 1$) of the amplitude of the central peak of the real part of the space-domain wavelet, then $|\mathbf{k}_0| = \pi\sqrt{2/\ln p}$. The $|\mathbf{k}_0|$ value used in this study is 2.668, which give a space-domain wavelet whose first sidelobes is 1/16 of the magnitude of the central amplitude (Kirby and Swain, 2011).

Table 1
Symbols and values of constants.

Constant	Symbol	Value	Units
Young's modulus	E	100	GPa
Poisson's ratio	υ	0.25	
Newtonian gravitational constant	G	6.67259×10^{-11}	$m^3\,kg^{-1}\,s^{-2}$
Gravity acceleration	g	9.79	$m\,s^{-2}$
Seawater density	ρ_w	1030	$kg\,m^{-3}$
Crust density	ρ_c	2670	$kg\,m^{-3}$
Mantle density	ρ_m	3300	$kg\,m^{-3}$

To recover T_e, the Bouguer gravity anomaly and topography are mirrored about their edges prior to Fourier transformation, which, when used with the wavelet transform does not generally bias the results significantly, as it can with the periodogram method (Kirby and Swain, 2008). The wavelet transform is then applied to both datasets to calculate the auto and cross-spectra at different azimuths and scales. We follow Kirby and Swain (2009) and invert the square of the real part of the wavelet coherency (SRC), rather than the coherence, because it is less sensitive to correlations between the initial loads on the plate and to "gravitational noise", both of which can cause incorrect recovery of T_e (Kirby and Swain 2009, 2011).

2.3. Regional topography, gravity and crustal structure

The elevation data used in our analysis are obtained from the ETOPO1 digital elevation model, a 1 arc-minute global relief model of Earth's surface that integrates land topography and ocean bathymetry (Amante and Eakins, 2009). Our area contains both continental and oceanic lithosphere, with the latter being subject to an additional water load. To treat mixed land and marine environments, we adopt the approach of Stark et al. (2003) and Kirby and Swain (2008). This approach scales ocean bathymetry (h) to an equivalent topography [$h' = (\rho_c - \rho_w)h/\rho_c$] prior to Fourier transformation, with subsequent application of the land loading deconvolution equations to the entire data set. Kirby and Swain (2008) showed that although this approach may bias T_e in ocean areas, the bias is small. Values of the densities are given in Table 1. The equivalent topography represents the bathymetry that would be expected if there were no water present (provided Airy isostasy operates). This allows the loading equations for a land environment to be used for the whole area, rather than performing two separate analyses and inversions on land and ocean areas (Pérez-Gussinyé et al., 2004).

The regional free-air gravity anomaly data are taken from the V18 Global Gravity Anomaly model of Sandwell and Smith (2009), on a $1' \times 1'$ grid over both land and ocean. The Bouguer gravity anomaly has been calculated applying the complete Bouguer correction at regional scales to free-air data using the FA2BOUG code (Fullea et al., 2008). We calculated terrain corrections using the ETOPO1 digital elevation model (see above), with a reduction density of 2670 $kg\,m^{-3}$. The Bouguer gravity anomaly of the study area obtained following this procedure is shown in Fig. 2.

The deconvolution requires detailed information on the internal structure of the crust and uppermost mantle. To define the internal density profile and lateral variation of the different interfaces, we use the global crustal model CRUST2.0 (Laske and Masters, 1997; Bassin et al., 2000; Laske et al., 2000). CRUST2.0 includes three crustal and two sediment layers, whose 7th layer describes the Moho depth. Forsyth's (1985) original formulation of the predicted coherence assumes that all internal density variations and loading occurs at the Moho. In this study we assumed that internal loading occurs at the interface between upper and mid-crust. Since the observed coherence can be reproduced equally well by either low T_e and shallow loading or a larger T_e and deeper loading, there

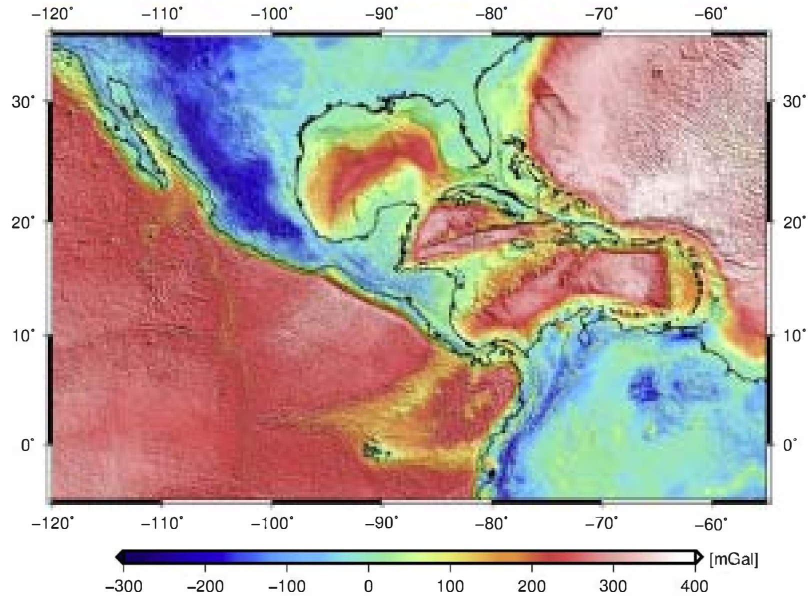

Fig. 2. Bouguer gravity anomaly used for the analysis. Topography shaded relief superimposed.

is a trade-off between T_e and assumed depth of loading. However, Pérez-Gussinyé and Watts (2005) tested the sensitivity of T_e to loading depth in Europe and found that changing the loading depth from the mid-crust to Moho changed T_e by ~5 km, but the general patterns of variations remained the same (Pérez-Gussinyé and Watts, 2005; Pérez-Gussinyé et al., 2007). Other constants are given in Table 1.

We project all data sets to a Cartesian coordinate system using the Mercator projection to mitigate errors arising from the planar treatment of curvilinear coordinates. The data cover a much larger area than the study area to mitigate boundary effects.

3. Results

3.1. Spatial variations of T_e

The effective elastic thickness obtained from the multitaper and wavelet methods are shown in Fig. 3. Fig. 3a shows the final T_e from multitaper method after merging results from three different window sizes. Fig. 3b shows T_e estimated from the wavelet method with $|\mathbf{k}_0| = 2.668$. In the following, we present our results and describe only those T_e variations present in the results obtained with both multitaper and wavelet methods.

The pattern of T_e variations in Central America and surrounding regions agrees well with the tectonic provinces in the area, and it is closely related to major tectonic boundaries (Fig. 3). The stable platforms of the North and South American plates have relatively high values. Otherwise, both methods give low values over the southern Cordillera and Baja California areas of North America. A steep T_e gradient separates this region from the southerly regions of the Interior Platform, which are characterized by intermediate to high T_e values (50–100 km). To the east, T_e decreases smoothly towards the Atlantic plain. Over northern South America, we also recover a high T_e within the stable platform. Both methods give very large values (>90 km) over the northern part of the Amazonia craton, where a linear SW–NE trending of much lower T_e values characterize the eastern part of the Guyana Shield within the rigid cratonic interior. Northward along the Northern Andes there is an increase of T_e to intermediate values at the junction with the boundary between the South American and Caribbean plates.

The northern part of the Maya block shows a linear SW–NE trend of intermediate to high T_e values. The Trans-Mexican Volcanic Belt is characterized by very low T_e values, which are bounded to the south by a narrower band of relatively higher T_e. The Maya–Chortis and Chortis–Chorotega active boundaries (i.e., the Polochic–Motagua Fault System and Santa Elena shear zone, respectively) show steep gradients with lower T_e values than the surrounding regions, such that the interaction between these blocks has reduced the strength of the lithosphere near their boundaries. Our results also show a linear NW–SE trending zone of low T_e associated with the Central American volcanic arc, probably associated with high heat flow related to magma transport along the arc (see below). Within the Chortis block, which shows low T_e values, there are two areas of relatively high T_e that coincide with the Nicaraguan depression and the eastern passive margin of this block.

Low to intermediate T_e values characterize the Eastern Pacific Ocean, where both methods give extremely low values (<5 km) along region under intensive extension and volcanism, e.g., the East Pacific Rise, around the Galapagos hotspot, Cocos Ridge, Carnegie Ridge and the Cocos–Nazca spreading center, as well as the Cayman spreading center in the Caribbean Sea. The Eastern Pacific also shows contrasting patches of high and low T_e. The Middle American subduction zone is characterized by a narrower band of high T_e on the downgoing slab, greater than 30 km, over the outer rise seaward of the trench. These T_e values decrease sharply under the Middle American Trench (MAT) offshore of Central America. In this zone, the Tehuantepec Ridge (TR) represents a major limit which separates the oceanic lithosphere into two distinct tectonic regions with a maximum T_e offset of ~30 km, such that seaward of the trench show higher T_e values in the northwest of the TR than to the southeast of the TR.

Over the Gulf of Mexico there is a linear SW–NE trend of intermediate to high T_e values (20–40 km) associated with old oceanic crust (seafloor ages of ~160–120 Myr; Müller et al., 2008) which outcrops in this area. Moreover, most of the Caribbean oceanic domain seems to be uniformly weak. In addition, several patches of intermediate to high T_e are also visible in the Colombian and Venezuelan basins. Westward, the Cocos–Nazca slab window beneath southeastern Costa Rica and northwestern Panamá is characterized by extremely low T_e (<4 km). Finally, T_e increases to

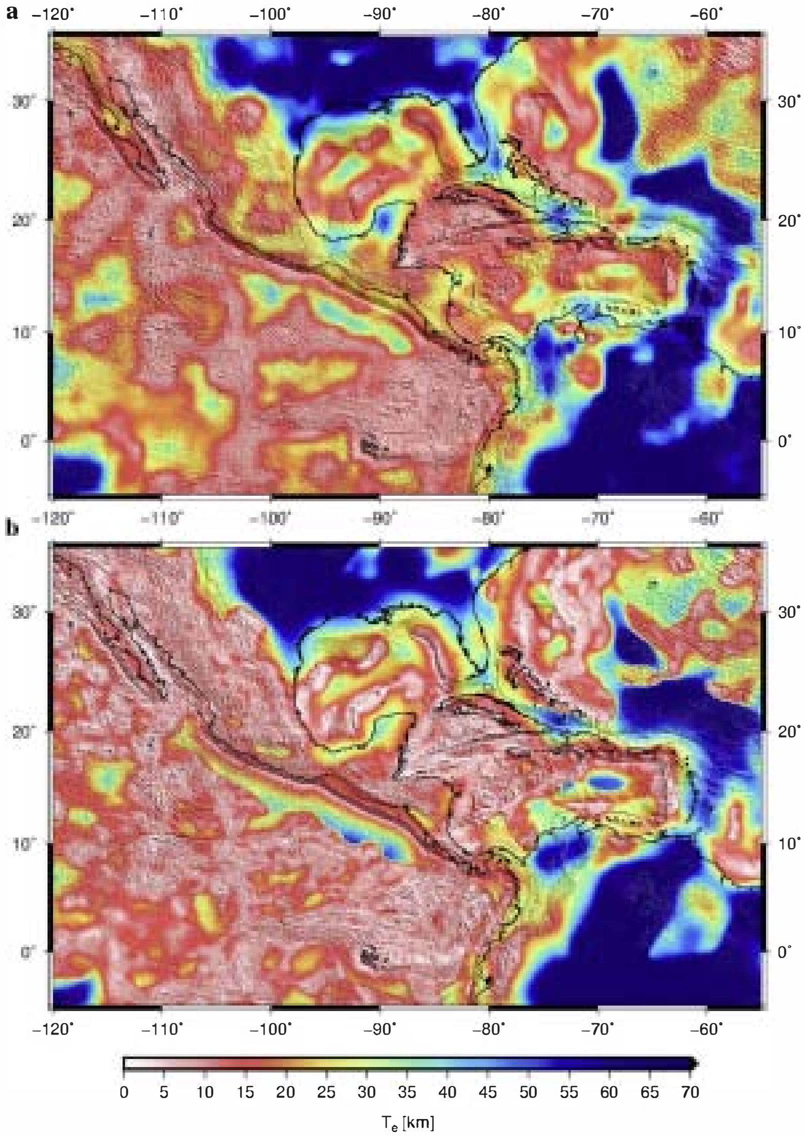

Fig. 3. Effective elastic thickness, T_e, over Central America and surrounding regions from: (a) multitaper method, and (b) wavelet method. In both images, topography shaded relief is superimposed. (a) shows final T_e after merging the results from the three different window sizes (see Section 2 and Supp. Fig. 1). The final T_e structure retains the primary characteristics of the largest window, but it better resolves the sharp gradient between low and high T_e areas and the short wavelength variations in T_e. (b) shows T_e estimated from the wavelet method with $|\mathbf{k}_0| = 2.668$.

high values clearly delineated along the transform plate boundary between the South American and Caribbean plates and Lesser Antilles Trench, which connect northward with the high T_e values in the Puerto Rico Trench, western North Atlantic margin and the Bermuda Rise region.

Regardless of the technical differences between the two methods, there is a good overall agreement in the relative spatial variations of T_e recovered from both techniques. Although absolute T_e values can vary in both maps, the qualitative T_e structure and location of the main T_e gradients are very similar. The greater discrepancies between both methods are local spatial variations of T_e in the stable platforms of the North and South American plates. Other differences are observed in T_e values recovered along the plate boundary between the South American and Caribbean plates, northward of the Lesser Antilles Trench and Bermuda Rise region. Since this study focuses on spatial variations of T_e and its geodynamic implications for Central America and surrounding regions, we do not discuss here the differences in absolute values between both maps produced by the methods, and the interested reader can find a more thorough comparison between the wavelet and multitaper methods in, for example, Daly et al. (2004), Audet et al. (2007), Pérez-Gussinyé et al. (2007, 2009a), and Kirby and Swain (2011).

As mentioned above, there are several 'key' parameters used in the analysis that lead to small (but perhaps significant) changes in resolution and accuracy of the results from both methods. Here we follow the approach of Pérez-Gussinyé et al. (2009b) and Kirby and Swain (2011) to obtain high spatial resolution and at the same time recover potentially high T_e from both methods. We have included an extensive description of the choice of parameters and its influence on the results, as well as the biases in T_e estimation, in the Supplementary Material. It should also be noted that "gravitational noise" (McKenzie and Fairhead, 1997; McKenzie, 2003; Kirby and Swain, 2009) does exist in the study area, which casts doubt upon T_e values in some regions, especially where we have recovered very high values; we will return to this issue in the Discussion.

3.2. Comparison with previous T_e estimates

Direct comparison of T_e values and its variations is possible between our results and the previous study of T_e from the multitaper method by Lowry and Pérez-Gussinyé (2011) for the western United States, and with T_e computed by Tassara et al. (2007) and Kirby and Swain (2011) for northern South America using $|\mathbf{k}_0| = 2.668$ and $|\mathbf{k}_0| = 5.336$ wavelets (Supp. Fig. 6 shows our results obtained from wavelet method with $|\mathbf{k}_0| = 5.336$). Our results are consistent with these and other previous regional studies of North America (Kirby and Swain, 2009), and South America (Pérez-Gussinyé et al. 2007, 2008, 2009a). This consistency indicates the viability of our results over Central America and surrounding regions.

Regarding the Central America region, there are numerous studies of oceanic T_e performed for given places (for a compilation see Watts, 2001). For the Middle America Trench, Caldwell and Turcotte (1979) estimated a T_e of 18.6 ± 2.2 km for seafloor age of 32.5 ± 2.5 Myr. Meanwhile, McNutt (1984) obtained a T_e of 17.5 ± 2.5 km for 20 ± 5 Myr, McAdoo and Martin (1984) a T_e of 29.7 ± 2.2 km for 20 ± 5 Myr, and Levitt and Sandwell (1995) a T_e of 27.3 ± 10 km for 19.9 ± 8 Myr. Feighner and Richards (1994) studied the Galápagos region using a variety of compensation models, obtaining a T_e of 12 ± 2 km and 3 ± 3 km for 7.5 ± 1 Myr. McAdoo et al. (1985) obtained a T_e of 31.7 ± 5.2 km for 80 ± 5 Myr over the Puerto Rico Trench, and Levitt and Sandwell (1995) a T_e of 40.7 ± 5 km for 101.6 ± 12 Myr over the Antilles Trench. Furthermore, in their study Manea et al. (2005) estimated T_e of the oceanic lithosphere beneath Tehuantepec Ridge by means of an admittance analysis of a set of profiles across this structure. These authors obtained a T_e of ~5–10 km in the NW area of the TR, while in the SE area T_e is of ~10–15 km. As mentioned above, we recover a complex pattern of T_e associated with the TR, with a maximum offset of ~30 km.

Finally, our results are in a good agreement with previous global studies as in e.g., Watts et al. (2006), who obtained T_e estimates from a wide range of submarine volcanic features in the East Pacific Ocean. Recently, Kalnins (2011) produced a global map of elastic thickness in the world's oceans, and recovered T_e at major constructional volcanic features in our study area, as the Bermuda Rise (T_e of 15–21 km), Carnegie Ridge (3–4 km), Cocos Ridge (3–4 km), Galapagos Islands (3–4 km) or Nazca Ridge (4–5 km). Furthermore, our results are also in a good agreement with the worldwide T_e map obtained by Audet and Bürgmann (2011) from the Bouguer coherence using the continuous wavelet transform, and with T_e results of Tesauro et al. (2012) from a rheological approach based on the lithospheric strength distribution, although our results have higher resolution due to the regional nature of the present work.

4. Discussion

4.1. T_e, surface heat flow and thermal age

Due to the dependence of lithosphere strength on temperature, T_e should show an inverse correlation with heat flow (McNutt, 1984; Lowry and Smith, 1995): higher surface heat flow implies higher lithospheric temperatures and hence lower lithospheric strength. Several studies examining the dependence of the strength of the lithosphere on the temperature structure (e.g., Watts and Burov, 2003; Afonso and Ranalli, 2004; Burov and Watts, 2006), found that there is not a simple relation between T_e and surface heat flow for continental areas, due to local differences in crustal structure and composition (which implies differences in radioactive heat production and thermal and rheological properties of the rocks) and lithosphere flexure (which affects the vertical distribution of elastic stresses). Otherwise, the situation is relatively simpler for oceanic areas, because oceanic crust is thinner and comparatively devoid of radioactive elements, implying that the strength of the lithosphere is mostly controlled by the cooling history (i.e., thermal age) of the oceanic lithosphere, although flexural effects can be important.

Fig. 4a shows the regional surface heat flow in the study area from the updated global heat flow database of the International Heat Flow Commission (Hasterok, 2010). Despite some uncertainties, there is a relatively good (inverse) correlation between surface heat flow and T_e values in Central America and surrounding regions. Low T_e values observed in the southern Cordillera and Baja California are associated with relatively high heat flow. Similarly, high T_e values recovered for southern regions of the Interior Platform match the observed low heat flow (Fig. 3 and Fig. 4a). By contrast, there are extensive areas with no measurements, e.g., the northern South America. Pérez-Gussinyé et al. (2007, 2008) examined the relationship of T_e to heat flow in South America, concluding that both parameters correlate well. Our relatively high T_e values observed in the northern part of the Maya block and in the southern boundary of the Trans-Mexican Volcanic Belt are well correlated with the low surface heat flow of these areas. The Trans-Mexican Volcanic Belt is characterized by intermediate to high heat flow and low T_e values. The southern Maya block and northwestern Chortis block, including the northwestern Central American volcanic arc, are also characterized by high surface heat flow and low T_e values. By contrast, the southeastern part of the Central American volcanic arc and Chorotega block are characterized by low heat flow and low T_e values (Fig. 3 and Fig. 4a), such that it's possible that due to the narrow width of the Central American land bridge in this area, the T_e recovered over the continent is very influenced by the low T_e values of the surrounding oceanic regions.

As illustrated in Fig. 4a, high heat flow is observed in the Eastern Pacific Ocean in regions under intensive extension and volcanism, e.g. the East Pacific Rise, around the Galapagos hotspot, Cocos Ridge, Carnegie Ridge and the Cocos–Nazca spreading center, as well as over the Cayman spreading center in the Caribbean Sea. This first-order pattern of surface heat flow variation is in accord with our low T_e estimates for these areas (Fig. 3). However, a low heat flow is observed within the Cocos plate where there is not a clear correlation with the T_e signature associated to the Middle American subduction zone (see below). The western Caribbean region shows moderate surface heat flow, where the Cocos–Nazca slab window beneath Central America, characterized by extremely low T_e, does not show a high surface heat flow. Meanwhile the eastern Caribbean region is characterized by lower values, with several contrasting patches of high surface heat flow as in the central part of the Hess Escarpment or over the Aves Ridge associated with the Lesser Antilles.

It is commonly accepted that T_e reflects a fossil lithospheric equilibrium developed at the time of loading (for a review see Artemieva, 2011). If loading occurs when the lithosphere is weak and no mass redistribution occurs afterwards, there is no need for stress to re-equilibrate, and isostatic analyses might yield a low T_e estimate even after subsequent cooling and strengthening of the lithosphere, as is the case for oceanic lithosphere (Pérez-Gussinyé et al., 2009b). Fig. 4b shows the age–area distribution of the ocean floor from Müller et al. (2008) in the study area. If we compare our T_e results with the age of the ocean crust in the study area (Fig. 4c), a direct relationship between them is not evident. This is consistent with the scatter observed in previous works on other oceanic regions (e.g., Tassara et al., 2007; Kalnins and Watts, 2009). Watts (2001) notes that the load age, which is not necessarily the same of the crust age, would explain much of this scatter. Other contributing sources could be

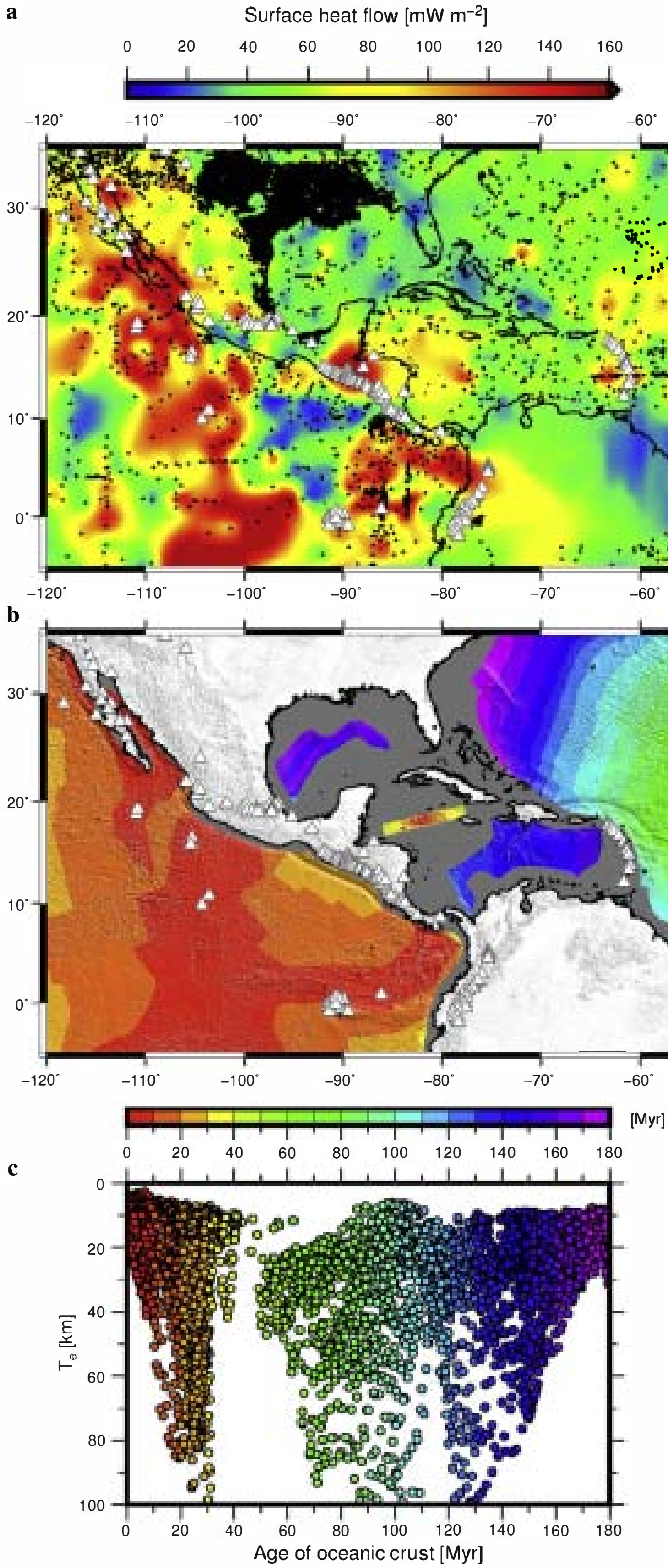

Fig. 4. (a) Regional surface heat flow from the updated global heat flow database of the International Heat Flow Commission (Hasterok, 2010). Black circles indicate measurement sites. White triangles show the position of Holocene volcanoes (Siebert and Simkin, 2002). (b) Age–area distribution of ocean floor from Müller et al. (2008). (c) Effective elastic thickness, T_e, from the multitaper method versus age of the oceanic crust (Müller et al., 2008).

uncertainties in load, infill and mantle densities, thermal perturbations due to hot and cold spots (e.g., Tassara et al., 2007), viscoelastic stress relaxation (Watts and Zhong, 2000), yielding in regions of large loads and high curvature (McNutt and Menard, 1982), or spatial variations in the controlling isotherms that determine T_e (Kalnins and Watts, 2009).

Otherwise, as stated above, the thermal state and rheological behavior of the lithosphere in continental areas are largely a consequence of local conditions, such that there is a complex relationship between T_e and the age of the continental lithosphere. Surface processes of erosion and deposition constantly redistribute continental surface mass loads. In any case, the high T_e values recovered here for the stable platforms of the North and South American plates (see Fig. 3) are consistent with previous studies for these regions (Tassara et al., 2007; Pérez-Gussinyé et al. 2007, 2009a; Kirby and Swain 2009, 2011).

4.2. Loading of the lithosphere

A fundamental assumption of the load deconvolution method developed by Forsyth (1985) is that surface and subsurface loads are statistically uncorrelated. In many cases, however, surface and subsurface loading are likely to be tectonically related processes and, therefore, spatially correlated (Forsyth, 1985). Subsurface loads include mafic intrusions, accreted lower crustal material, thermal anomalies and compositional variations, which cause lateral variations of density at depth and may have a strong influence on T_e estimates (Stark et al., 2003). Meanwhile, surface loading is caused by topography and large-scale variations in surface density (e.g., mountains and sedimentary basin). Macario et al. (1995) showed that when the degree of correlation of initial surface and subsurface loading increases, the T_e values estimated using Forsyth's (1985) deconvolution method can be biased downward. Furthermore, erosion and sedimentation may play an important role in modifying the relationship between surface topography and subsurface density anomalies (e.g., Forsyth, 1985; McKenzie and Fairhead, 1997). Both processes can reduce the landscape to a perfectly flat surface, removing the topographic expression of subsurface loads. The presence of topographically unexpressed internal loading, known as "noise" or "gravitational noise" (McKenzie and Fairhead, 1997; McKenzie, 2003; Kirby and Swain, 2009), biases the T_e upward. As pointed out by Kirby and Swain (2009), this problem can occur in regions of subdued topography, and predominantly affects areas where the coherence method indicates high T_e (see Suppl. Fig. 7).

The load deconvolution wavelet method can also estimate the ratio between the initial internal and surface load amplitudes (the loading ratio, f; Forsyth, 1985). We can display the loading ratio results in terms of the F parameter, the internal load fraction (McKenzie, 2003), where purely surface loading gives $F = 0$, purely internal loading gives $F = 1$, while equal surface and internal loading gives $F = 0.5$ (see Supplementary Material for an extended explanation). Fig. 5a shows best fitting F values corresponding to the T_e recovered from the wavelet method (Fig. 3b). For North America, our results are consistent with Kirby and Swain's (2009) F results, which show that subsurface loading has dominated continental tectonics, or at least been equal in magnitude to surface loading, in North America. Our results are also consistent with the pattern of the flexural loading ratio, f_F, obtained by Tassara et al. (2007) in northern South America, which suggest that below the north–eastern limit of the Amazonia craton there are strong lateral variations in density not compensated by surface topography. Subsurface loading dominates along the East Pacific Rise, around the Galapagos hotspot, Cocos Ridge, Carnegie Ridge and the Cocos–Nazca spreading center (Fig. 5a). In this zone, the Tehuantepec Ridge represents, again, a major limit which separates the oceanic lithosphere into two distinct load regions, such that the northwest TR is dominated by surface loading while the southeast TR is dominated by internal loads. The Caribbean region is characterized by all range of F values. Higher F values are observed over the eastern Cayman spreading center, the Caribbean Large Igneous Province, the Cocos–Nazca slab window beneath Central America, the Aves Ridge, and along the Lesser Antilles Trench and east North American margin.

Fig. 5b shows seafloor sediment thickness (Divins, 2003; Whittaker et al., 2013) in the study area. Large amount of sediments are located on the Gulf of Mexico basin, along of the western North Atlantic margin, the Colombian, Venezuelan and Grenada basins, and on the Barbados Accretionary Complex associated to the Lesser Antilles. In many cases sediment thickness exceeds 10 km. However, most of the Caribbean lithosphere, where both methods recovered low T_e values (see Fig. 3), seems to be uniformly weak, suggesting that the effect of the sediments on T_e estimates is very small. The continental shelf of the Gulf of Mexico, which shows a smooth surface, is characterized by moderate to high T_e values (between 40 and 50 km; see Fig. 3) and low F values, with surface loads dominating. Seaward, high T_e values are recovered for the Mississippi delta system (Fig. 3). Southwestward in the Gulf of Mexico, over the old oceanic crust which outcrops in this area, both methods recover a linear SW–NE trending of intermediate to high T_e values associated with a high F value. The Venezuelan basin also shows high T_e values associated with a subsurface loading domain, possibly related to the oceanic basement underneath the Caribbean Large Igneous Province. Müller et al. (2008) found prominent negative residual basement depth anomalies (in a range between 750 and 1500 m) associated with the Gulf of Mexico, northeast of Venezuela, and off the east coast of North America, which may be related to subducted slab material descending in the mantle or to asthenospheric flow. In the case of the Colombian basin, the presence of sediments on the continental shelf may play a major role on the estimation of T_e (~40 km; Fig. 3 and Fig. 5b). Interestingly, the presently active Nicaraguan depression, which experienced significant extension in the Cenozoic, shows intermediate T_e values (~25 km) and a F value of 0.5, such that it is possible that in this case T_e values are overestimated due to the effect associated with its sediment fill (see Suppl. Fig. 7).

4.3. The Middle American and Lesser Antilles subduction zones

The results over the Middle American and Lesser Antilles subduction zones should be interpreted with caution. As exposed in the Results Section, the Middle American subduction zone is characterized by a narrower band of high T_e on the downgoing slab seaward of the trench (Fig. 3). These T_e values decrease sharply under the MAT offshore of Central America, indicating a substantial degree of weakening within the downgoing plate due to the flexure of the lithosphere (see McNutt and Menard, 1982; Judge and McNutt, 1991; Billen and Gurnis, 2005; Contreras-Reyes and Osses, 2010). In fact, the bathymetry of the MAT offshore of Central America shows a complex response of the crust to the subduction process, with widespread outer-rise normal faulting subparallel to the trench axis due to the plate bending, increasing in number and offset where the bending is more pronounced (Ranero et al. 2003, 2005; Harders et al., 2011; Manea et al., 2013). This high T_e signature is very evident (broader and even exceeding 50 km at the Lesser Antilles Trench; see Fig. 3), and can also be observed in other subduction zones, as e.g. along the Peru–Chile Trench (Tassara et al., 2007; Pérez-Gussinyé et al., 2009a; Kirby and Swain, 2011), or over the Japan, Izu–Bonin, and Mariana trenches and at the northernmost tip of the Tonga–Kermadec trench (Kalnins and Watts, 2009).

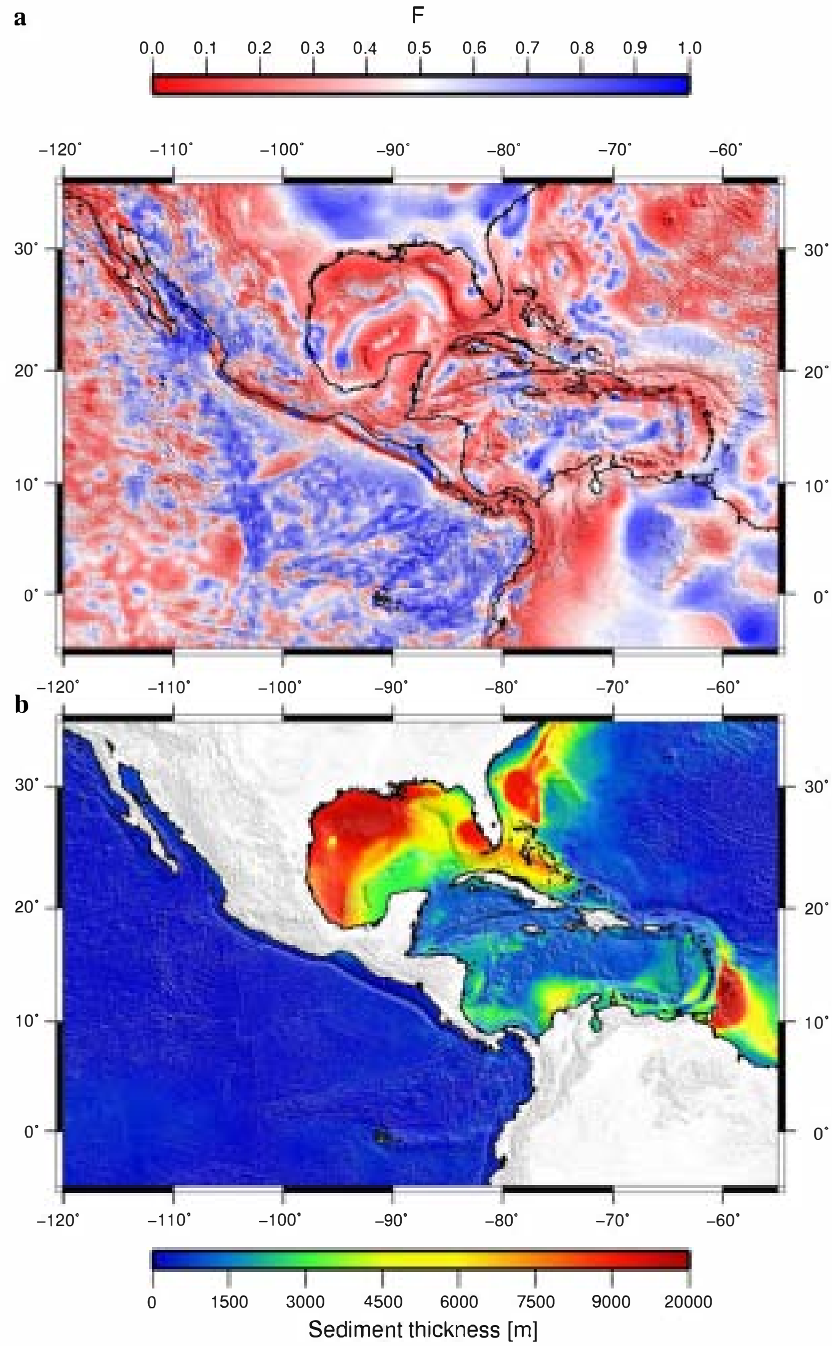

Fig. 5. (a) Loading ratio (F) corresponding to the T_e obtained from the wavelet method (Fig. 3b). (b) Sediment thickness (meters) on the seafloor in the study area from the 5 arc-minute digital total-sediment-thickness database for the world's oceans and marginal seas (Divins, 2003; Whittaker et al., 2013).

Subsurface loads, such as those due to a dense downgoing slab, should be taken into account when interpreting the results over subduction zones (Kalnins and Watts, 2009). We have found that the high T_e values over the Middle American and Lesser Antilles subduction zones are dominated by internal loads (and in the case of the southernmost tip of the LAT also associated with a large amount of sediments; see Fig. 5), where the corresponding noise levels are high (see Suppl. Fig. 7) and thus, these results may be biased upward. If T_e over the Middle American subduction zone is actually low (at least relatively), it would be in accordance with they reflecting a "frozen in" signal which is not affected in this zone by subsequent cooling and strengthening of the oceanic lithosphere. Interestingly, this is not the case of the Lesser Antilles subduction zone, where the high T_e values are free of noise (excepting the southernmost tip of the LAT associated with a large amount of sediments; see Fig. 5b and Suppl. Fig. 7), and persist in all our results from different window sizes and $|\mathbf{k}_0|$ in both multitaper and wavelet methods, respectively (see Fig. 3 and Supp. Figs. 1 and 6). This is in accordance with the strength of the oceanic lithosphere is being in this case controlled by the thermal age of the lithosphere at the time of loading (Watts, 2001; Kalnins and Watts, 2009), such that T_e values increase with cooling of the oceanic lithosphere away from the ridge. Furthermore, it should be noted that the results over the Middle American and Lesser Antilles subduction zones, especially in relation to the high gradient that limits these bands of higher T_e, are highly dependent on the choice of spectral parameters in both multitaper and wavelet methods (see Fig. 3 and Supp. Figs. 1 and 6).

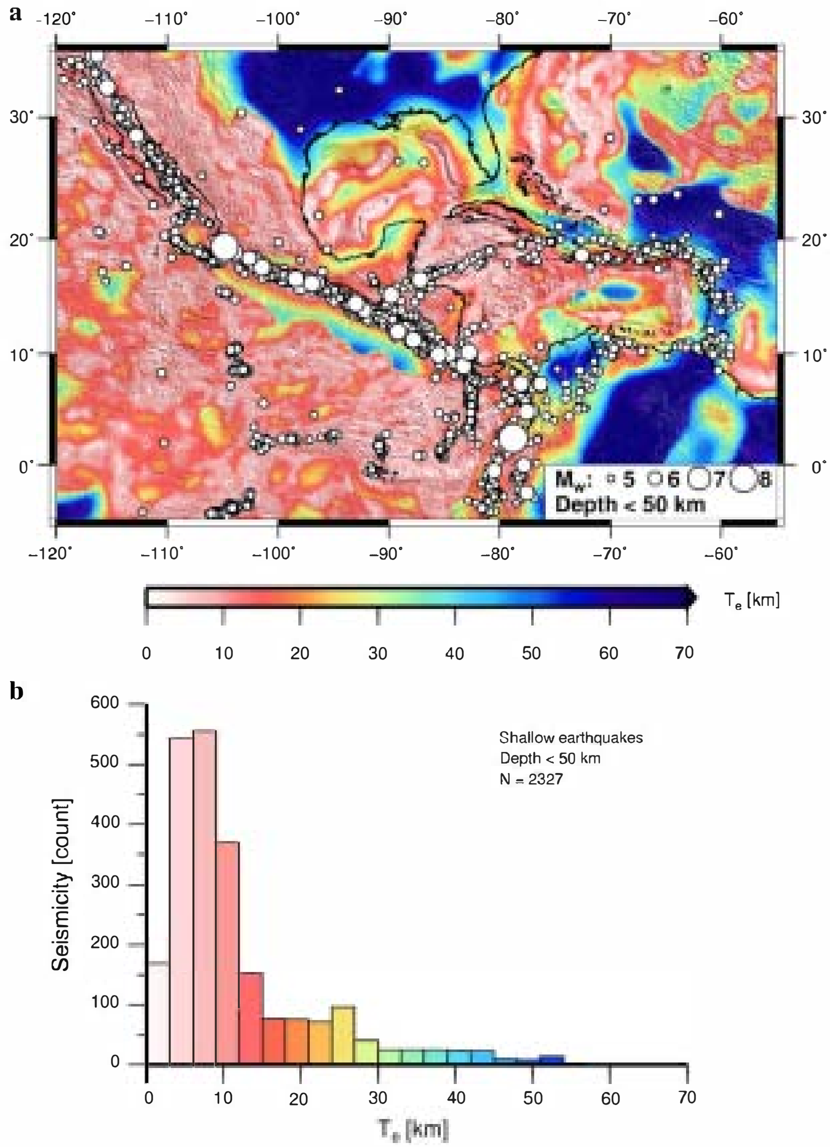

Fig. 6. (a) Correlation between distribution of the shallow seismicity (depth <50 km) from the Global CMT seismic catalog (Ekström et al., 2012) with T_e derived from the wavelet method. (b) Histogram shows shallow earthquake events versus T_e.

4.4. T_e and seismicity

The magnitude and spatial variations of T_e could control the degree, style and localization of deformation in response to long-term tectonic loads, and potentially the distribution of seismic activity (e.g., Lowry and Smith, 1995; Tassara et al., 2007; Audet and Bürgmann, 2011; Chen et al., 2013). The seismotectonics of the circum-Caribbean area is complex, and essentially related to plate boundaries, with intraplate activity being very scarce (Fig. 6a). Comparison of the spatial variation of T_e with the shallow (<50 km deep) earthquake distribution indicates that most of the seismic activity is located in regions with low T_e or steep T_e gradient, while the lack of seismicity in stable tectonic provinces characterized by high T_e values is evident (Fig. 6a). As illustrated in Fig. 6b, shallow earthquakes are very frequent in regions with low T_e (<20 km), and are relatively scarce in regions with higher values. This suggests that the stronger lithosphere resists deformation and transfers the stress effectively, while the weak lithosphere and areas with steep change of T_e are prone to accumulate and then release tectonic stresses causing earthquakes (Mao et al., 2012; Chen et al., 2013).

5. Conclusions

We have used two different spectral methods (multitaper and wavelet) to calculate the coherence between the Bouguer gravity anomaly and the topography in order to estimate the spatial variations in effective elastic thickness in Central America and surrounding regions. We have generated, for the first time, high-resolution maps of spatial variations of T_e for this region. Regardless of the technical differences between the two methods, there is a good overall agreement in the spatial variations of T_e recovered from both methods. Although absolute T_e values can vary in both maps, the qualitative T_e structure and location of the main T_e gradients are very similar, such that estimation of T_e is relatively insensitive to the choice of spectral estimator.

The pattern of the T_e variations in Central America and surrounding regions agrees well with the tectonic provinces in the region, and it is closely related to major tectonic boundaries. There is a relatively good correlation, despite some uncertainties, between surface heat flow and our T_e results. These results suggest that although this area is geologically complex, the thermal state of the lithosphere has profound influence on its strength, such that

T_e is strongly governed by thermal structure. Otherwise, in general there is not a direct relationship between T_e and the age of the ocean crust in of our study area (contrary to that expected if T_e is exclusively controlled by the thermal structure of the oceanic lithosphere), which could be explained for other factors, maybe mainly differences in age loading.

The Middle American and Lesser Antilles subduction zones are characterized by a band of high T_e on the downgoing slab seaward of the trenches. These high T_e values are related to internal loads (and in the case of the southernmost tip of the LAT also associated with a large amount of sediments); showing high noise levels and they may be biased upward. Thus, the results over subduction zones should be interpreted with caution, and warrant further analysis.

Finally, future research should also evaluate the relationship between T_e, as well as its anisotropy, Moho structure and mantle structure within a geodynamical perspective, in order to improve our understanding on the evolution of the Caribbean plate.

Acknowledgements

We thank Pascal Audet, an anonymous reviewer, and Editor Yanick Ricard for their useful reviews that significantly improved this manuscript. We also thank Javier Fullea for providing the FA2BOUG code. A.J.-D. especially thanks Pilar Llanes and Yangfan Deng for fruitful discussion on various topics of the methodology. The figures have been produced with the GMT software (Wessel et al., 2013). A.J.-D. work was supported by a grant of the Universidad Complutense de Madrid. J.R. work was supported by a contract Ramón y Cajal co-financed from the Ministerio de Economía y Competitividad of Spain and the European Social Fund. This work was carried out in the projects CGL2008-03463 and CGL2009-14405-C02-02. This work is a contribution from the Active Tectonics, Paleoseismology and Associated Hazards research group (UCM-910368; http://tectact.wordpress.com/).

Appendix A. Supplementary material

Supplementary material related to this article can be found online at http://dx.doi.org/10.1016/j.epsl.2014.01.042.

References

Addison, P.S., 2002. The Illustrated Wavelet Transform Handbook. Institute of Physics Publishing, Bristol, UK.

Afonso, J.C., Ranalli, G., 2004. Crustal and mantle strengths in continental lithosphere: is the jelly sandwich model obsolete?. Tectonophysics 394, 221–232.

Amante, C., Eakins, B.W., 2009. ETOPO1 1 arc-minute global relief model: procedures, data sources and analysis. NOAA Technical Memorandum NESDIS NGDC-24. 19 pp.

Artemieva, I., 2011. The Lithosphere: An Interdisciplinary Approach, vol. 773. Cambridge University Press. 773 pp.

Audet, P., Bürgmann, R., 2011. Dominant role of tectonic inheritance in supercontinent cycles. Nat. Geosci. 4, 184–187.

Audet, P., Jellinek, A.M., Uno, H., 2007. Mechanical controls on the deformation of continents at convergent margins. Earth Planet. Sci. Lett. 264, 151–166.

Bassin, C., Laske, G., Masters, T.G., 2000. The current limits of resolution for surface wave tomography in North America. Eos Trans. AGU 81, F897.

Billen, M.I., Gurnis, M., 2005. Constraints on subducting plate strength within the Kermadec trench. J. Geophys. Res. 110, B05407.

Bird, P., 2003. An updated digital model of plate boundaries. Geochem. Geophys. Geosyst. 4 (3), 1027. http://dx.doi.org/10.1029/2001GC000252.

Bürgmann, R., Dresen, G., 2008. Rheology of the lower crust and upper mantle: evidence from rock mechanics, geodesy, and filed observations. Annu. Rev. Earth Planet. Sci. 36, 531–567.

Burov, E.B., 2011. Rheology and strength of the lithosphere. Mar. Pet. Geol. 28, 1402–1443.

Burov, E.B., Diament, M., 1995. The effective elastic thickness of (Te) continental lithosphere. What does it really means?. J. Geophys. Res. 100 (B3), 3905–3927.

Burov, E.B., Watts, A.B., 2006. The long-term strength of continental lithosphere: "jelly sandwich" or "crème brûlée"?. GSA Today 16 (1), 4–10.

Caldwell, J.G., Turcotte, D.L., 1979. Dependence of the elastic thickness of the oceanic lithosphere on age. J. Geophys. Res. 84, 7572–7576.

Chen, B., Chen, C., Kaban, M.K., Du, J., Liang, Q., Thomas, M., 2013. Variations of the effective elastic thickness over China and surroundings and their relation to the lithosphere dynamics. Earth Planet. Sci. Lett. 363, 61–72.

Contreras-Reyes, E., Osses, A., 2010. Lithospheric flexure modeling seaward of the Chile trench: implications for oceanic plate weakening in the Trench Outer Rise region. Geophys. J. Int. 182 (1), 97–112.

Daly, E., Brown, C., Stark, C.P., Ebinger, C.J., 2004. Wavelet and multitaper coherence methods for assessing the elastic thickness of the Irish Atlantic margin. Geophys. J. Int. 159, 445–459.

DeMets, C., Gordon, R.G., Argus, D.F., 2010. Geologically current plate motions. Geophys. J. Int. 181, 1–80. http://dx.doi.org/10.1111/j.1365-246X.2009.04491.x. See also: Erratum. Geophys. J. Int. 187 (2011) 538. http://dx.doi.org/10.1111/j.1365-246X.2011.05186.x.

Divins, D.L., 2003. Total Sediment Thickness of the World's Oceans & Marginal Seas. NOAA National Geophysical Data Center, Boulder, CO.

Ekström, G., Nettles, M., Dziewoński, A., 2012. The global CMT project 2004–2010: centroid-moment tensors for 13,017 earthquakes. Phys. Earth Planet. Inter. 200–201, 1–9.

Feighner, M.A., Richards, M.A., 1994. Lithospheric structure and compensation mechanism of the Galápagos Arc. J. Geophys. Res. 99, 6711–6729.

Forsyth, D.W., 1985. Subsurface loading estimates of the flexural rigidity of continental lithosphere. J. Geophys. Res. 90, 12,623–12,632.

Fullea, J., Fernàndez, M., Zeyen, H., 2008. FA2BOUG – A FORTRAN 90 code to compute Bouguer gravity anomalies from gridded free air anomalies: application to the Atlantic–Mediterranean transition zone. Comput. Geosci. 34, 1665–1681.

Harders, R., Ranero, C.R., Weinrebe, W., Behrmann, J.H., 2011. Submarine slope failures along the convergent continental margin of the Middle America Trench. Geochem. Geophys. Geosyst. 12, Q05S32.

Hasterok, D., 2010. Thermal state of the Oceanic and Continental lithosphere. Ph.D. Thesis. University of Utah.

Hasterok, D., Chapman, D.S., 2011. Heat production and geotherms for the continental lithosphere. Earth Planet. Sci. Lett. 307, 59–70.

Judge, A.V., McNutt, M.K., 1991. The relationship between plate curvature and elastic plate thickness: a study of the Peru–Chile trench. J. Geophys. Res. 96 (B10), 16625–16639.

Kalnins, L.M., 2011. Spatial variations in the effective elastic thickness of the lithosphere and their tectonic implications. Ph.D. Thesis. University of Oxford.

Kalnins, L.M., Watts, A.B., 2009. Spatial variations in effective elastic thickness in the Western Pacific Ocean and their implications for Mesozoic volcanism. Earth Planet. Sci. Lett. 286, 89–100.

Kirby, J.F., Swain, C.J., 2008. An accuracy assessment of the fanwavelet coherence method for elastic thickness estimation. Geochem. Geophys. Geosyst. 9 (3), Q03022. Correction: Geochem. Geophys. Geosyst. 9 (5) (2008) Q05021.

Kirby, J.F., Swain, C.J., 2009. A reassessment of spectral Te estimation in continental interiors: the case of North America. J. Geophys. Res. 114, B08401.

Kirby, J.F., Swain, C.J., 2011. Improving the spatial resolution of effective elastic thickness estimation with the fan wavelet transform. Comput. Geosci. 37, 1345–1354.

Laske, G., Masters, G., 1997. A global digital map of sediment thickness. Eos Trans. AGU 78, F483.

Laske, G., Masters, G., Reif, C., 2000. A new global crustal model at 2 × 2 degrees (CRUST2.0). http://igppweb.ucsd.edu~gabi/rem.dir/crust/crust2.html.

Levitt, D.A., Sandwell, D.T., 1995. Lithospheric bending at subduction zones based on depth soundings and satellite gravity. J. Geophys. Res. 100, 379–400.

Lowry, A.R., Pérez-Gussinyé, M., 2011. The role of crustal quartz in controlling Cordilleran deformation. Nature 471 (7338), 353–357. http://dx.doi.org/10.1038/nature09912.

Lowry, A.R., Smith, R.B., 1995. Strength and rheology of the western U.S. Cordillera. J. Geophys. Res. 100, 17,947–17,963.

Lowry, A.R., Ribe, N.M., Smith, R.B., 2000. Dynamic elevation of the Cordillera, western United States. J. Geophys. Res. 105, 23,371–23,390.

Macario, A., Malinverno, A., Haxby, W.F., 1995. On the robustness of elastic thickness estimates obtained using the coherence method. J. Geophys. Res. 100 (D8), 15,163–15,172.

Manea, M., Manea, V.C., Kostoglodov, V., Guzman-Speziale, M., 2005. Elastic thickness of the lithosphere below the Tehuantepec Ridge. Geofis. Int. 44, 2157–2168.

Manea, V.C., Manea, M., Ferrari, L., 2013. A geodynamical perspective on the subduction of Cocos and Rivera plates beneath Mexico and Central America. Tectonophysics 609, 56–81.

Mao, X., Wang, Q., Liu, S., Xu, M., Wang, L., 2012. Effective elastic thickness and mechanical anisotropy of South China and surrounding regions. Tectonophysics 550–553, 47–56.

Mareschal, J.-C., Jaupart, C., 2013. Radiogenic heat production, thermal regime and evolution of Continental Crust. Tectonophysics 609, 524–534.

McAdoo, D.C., Martin, C.F., 1984. Seasat observation of geoid anomalies due to subducting slabs. J. Geophys. Res. 87, 8684–8692.

McAdoo, D.C., Martin, C.F., Poulose, S., 1985. Seasat observations of flexure: Evidence for a strong lithosphere. Tectonophysics 116, 209–222.

McKenzie, D., 2003. Estimating Te in the presence of internal loads. J. Geophys. Res. 108 (B9), 2438.

McKenzie, D.P., Fairhead, J.D., 1997. Estimates of the effective elastic thickness of the continental lithosphere from Bouguer and free air gravity anomalies. J. Geophys. Res. 102 (B12), 27523–27552.

McNutt, M.K., 1984. Lithospheric flexure and thermal anomalies. J. Geophys. Res. 89 (11), 11180–11194.

McNutt, M.K., Menard, H.W., 1982. Constraints on yield strength in the oceanic lithosphere derived from observations of flexure. Geophys. J. R. Astron. Soc. 71, 363–394.

Müller, R.D., Sdrolias, M., Gaina, C., Roest, W.R., 2008. Age, spreading rates, and spreading asymmetry of the world's ocean crust. Geochem. Geophys. Geosyst. 9, Q04006.

Percival, D.B., Walden, A.T., 1993. Spectral Analysis for Physical Applications, Multitaper and Conventional Univariate Techniques. Cambridge Univ. Press, New York, pp. 1–190.

Pérez-Gussinyé, M., Watts, A.B., 2005. The long-term strength of Europe and its implications for plate forming processes. Nature 436, 381–384.

Pérez-Gussinyé, M., Lowry, A.R., Watts, A.B., Velicogna, I., 2004. On the recovery of the effective elastic thickness using spectral methods: examples from synthetic data and from the Fennoscandian Shield. J. Geophys. Res. 109.

Pérez-Gussinyé, M., Lowry, A.R., Watts, A.B., 2007. Effective elastic thickness of South America and its implications for intracontinental deformation. Geochem. Geophys. Geosyst. 8 (5), Q05009.

Pérez-Gussinyé, M., Lowry, A.R., Phipps Morgan, J., Tassara, A., 2008. Effective elastic thickness variations along the Andean margin and their relationship to subduction geometry. Geochem. Geophys. Geosyst. 9, Q02003.

Pérez-Gussinyé, M., Swain, C.J., Kirby, J.F., Lowry, A.R., 2009a. Spatial variations of the effective elastic thickness, Te, using multitaper spectral estimation and wavelet methods: examples from synthetic data and application to South America. Geochem. Geophys. Geosyst. 10, Q04005.

Pérez-Gussinyé, M., Metois, M., Fernández, M., Vergés, J., Fullea, J., Lowry, A.R., 2009b. Effective elastic thickness of Africa and its relationship to other proxies for lithospheric structure and surface tectonics. Earth Planet. Sci. Lett. 287, 152–167.

Ranalli, G., 1997. Rheology of the lithosphere in space and time. Geol. Soc. (Lond.) Spec. Publ. 121, 19–37.

Ranero, C.R., Morgan, J.P., McIntosh, K., Reichert, C., 2003. Bending-related faulting and mantle serpentinization at the Middle America trench. Nature 425, 367–373.

Ranero, C.R., Villaseñor, A., Morgan, J.P., Weinrebe, W., 2005. Relationship between bend-faulting at trenches and intermediate-depth seismicity. Geochem. Geophys. Geosyst. 6, Q12002.

Ross, M.I., Scotese, C.R., 1988. A hierarchical tectonic model of the Gulf of Mexico and Caribbean region. Tectonophysics 155, 139–168.

Sandwell, D.T., Smith, W.H.F., 2009. Global marine gravity from retracked Geosat and ERS-1 altimetry: ridge segmentation versus spreading rate. J. Geophys. Res. 114, B01411.

Siebert, L., Simkin, T., 2002. Volcanoes of the world: an illustrated catalog of Holocene volcanoes and their eruptions. In: Smithsonian Institution, Global Volcanism Program Digital Information Series, GVP-3. http://www.volcano.si.edu/world/.

Simons, F.J., Zuber, M.T., Korenaga, J., 2000. Isostatic response of the Australian lithosphere: estimation of effective elastic thickness and anisotropy using multitaper spectral analysis. J. Geophys. Res. 105 (B8), 19,163–19,184.

Stark, C.P., Stewart, J., Ebinger, C.J., 2003. Wavelet transform mapping of effective elastic thickness and plate loading: validation using synthetic data and application to the study of southern African tectonics. J. Geophys. Res. 108 (B12), 2558.

Sykes, L.R., McCann, W.R., Kafka, A.L., 1982. Motion of Caribbean Plate during last 7 million years and implications for early Cenozoic movements. J. Geophys. Res. 87 (B13), 10656–10676.

Tassara, A., Swain, C.J., Hackney, R.I., Kirby, J.F., 2007. Elastic thickness structure of South America estimated using wavelets and satellite-derived gravity data. Earth Planet. Sci. Lett. 253, 17–36.

Tesauro, M., Kaban, M.K., Cloetingh, S.A.P.L., 2012. Global strength and elastic thickness of the lithosphere. Glob. Planet. Change 90–91, 51–57.

Thomson, D.J., 1982. Spectrum estimation and harmonic-analysis. Proc. IEEE 70 (9), 1055–1096.

Walden, A.T., McCoy, E.J., Percival, D.B., 1995. The effective bandwidth of a multitaper spectral estimator. Biometrika 82 (1), 201–214.

Watts, A.B., 2001. Isostasy and Flexure of the Lithosphere. Cambridge University Press. 472 pp.

Watts, A.B., Burov, E.B., 2003. Lithospheric strength and its relation to the elastic and seismogenetic layer thickness. Earth Planet. Sci. Lett. 213, 113–131.

Watts, A.B., Zhong, S., 2000. Observations of flexure and the rheology of oceanic lithosphere. Geophys. J. Int. 142 (3), 855–875.

Watts, A.B., Sandwell, D.T., Smith, W.H.F., Wessel, P., 2006. Global gravity, bathymetry, and the distribution of submarine volcanism through space and time. J. Geophys. Res. 111 (B8).

Wessel, P., Smith, W.H.F., Scharroo, R., Luis, J.F., Wobbe, F., 2013. Generic mapping tools: Improved version released. Eos Trans. AGU 94, 409–410.

Whittaker, J., Goncharov, A., Williams, S., Müller, R.D., Leitchenkov, G., 2013. Global sediment thickness dataset updated for the Australian–Antarctic Southern Ocean. Geochem. Geophys. Geosyst. 14 (8), 2547–3313. http://dx.doi.org/10.1002/ggge.20181.